Journal of Alloys and Compounds 860 (2021) 158436

Contents lists available at ScienceDirect

Journal of Alloys and Compounds

journal homepage: www.elsevier.com/locate/jalcom

$Al_{0.3}Cr_xFeCoNi$ high-entropy alloys with high corrosion resistance and good mechanical properties

Xiaolei Yan[a], Hui Guo[a], Wei Yang[a], Shujie Pang[a,b,*], Qing Wang[c], Ying Liu[a], Peter K. Liaw[d], Tao Zhang[a,**]

[a] Key Laboratory of Aerospace Materials and Performance (Ministry of Education), School of Materials Science and Engineering, Beihang University, Beijing 100191, China
[b] Beijing Advanced Innovation Center for Biomedical Engineering, Beihang University, Beijing 100191, China
[c] Key Laboratory of Materials Modification by Laser, Ion and Electron Beams (Ministry of Education), School of Materials Science and Engineering, Dalian University of Technology, Dalian 116024, China
[d] Department of Materials Science and Engineering, The University of Tennessee, Knoxville, TN 37996, USA

ARTICLE INFO

Article history:
Received 15 August 2020
Received in revised form 17 December 2020
Accepted 20 December 2020
Available online 31 December 2020

Keywords:
High-entropy alloy
Microstructure
Corrosion
Mechanical property

ABSTRACT

The effects of the Cr content on microstructure, corrosion behavior, and mechanical properties of the $Al_{0.3}Cr_xFeCoNi$ high-entropy alloys (HEAs) were studied. The $Al_{0.3}Cr_xFeCoNi$ alloys with x = 0–1.0 exhibited the single face-centered-cubic (FCC) structure, and the alloys with x = 1.5–2.0 consisted of the FCC and disordered body-centered-cubic (BCC)/ordered BCC (B2) structure. In the 3.5 mass% NaCl solution, the $Al_{0.3}Cr_xFeCoNi$ alloys are spontaneously passivated, and the pitting resistance of the alloys was improved with increasing the Cr content in the alloys. It is notable that the $Al_{0.3}Cr_xFeCoNi$ (x = 1.5–2.0) alloys with Cr-rich FCC and BCC phases demonstrated excellent pitting-corrosion resistance and low corrosion rates of less than 10^{-3} mm/year due to the formation of the protective surface films enriched in Cr_2O_3. Moreover, the $Al_{0.3}Cr_xFeCoNi$ (x = 0–1.0) alloys with the FCC structure exhibited relatively-low tensile strength and large elongation. The further increase in the Cr content to x = 1.5–2.0 improved the strengths and hardness of the alloys due to the increase in BCC/B2 phases. The $Al_{0.3}Cr_xFeCoNi$ (x = 1.5–2.0) alloys with high corrosion resistance presented good mechanical properties, including tensile strengths of 640–1078 MPa and tensile elongations of 11–44%. It is also demonstrated that increasing the Cr content of Al–Cr–Fe–Co–Ni HEAs is an effective approach for tailoring corrosion-resistant HEAs.

1. Introduction

High-entropy alloys (HEAs) are a new class of metallic materials consisting of five or more elements in equal or near-equal molar ratios, which favor the formation of simple crystalline structure, such as face-centered-cubic (FCC), body-centered-cubic (BCC), and hexagonal-close-packed (HCP) solid solutions [1–5]. Among the HEAs, the Al–Cr–Fe–Co–Ni alloys have attracted attention due to their good mechanical properties induced by the microstructural and compositional diversity [4–6]. For the $Al_xCrFeCoNi$ system HEAs, the crystalline structure could transform from an FCC phase to duplex FCC + BCC structure, and then to BCC/B2 phases with increasing the Al content [7–10]. This microstructural evolution of Al–Cr–Fe–-Co–Ni HEAs can also be achieved through changing the mixed ratios of the transition metals (TMs) [11], as evidenced by the facts that the addition of Fe, Co, and Ni with a certain amount could lead to the formation of the FCC solid solution [12–16], while Cr promoted the formation of the BCC phase [17,18]. Notably, the Al–Cr–Fe–Co–Ni HEAs with the duplex FCC + BCC structure exhibited a good strength–ductility combination, and are attractive as promising structural materials [19–24].

The microstructure and phase compositions of Al–Cr–Fe–Co–Ni HEAs also influence their corrosion behavior. It has been reported that for the $Al_xCrFeCoNi$ HEAs with duplex FCC + BCC structure, the Cr content in the BCC phase was lower than that in the FCC phase, and the nominal Cr contents of the alloys, and the deficiency of Cr in the BCC phase caused pitting corrosion at the BCC phase in the NaCl

* Corresponding author at: Key Laboratory of Aerospace Materials and Performance (Ministry of Education), School of Materials Science and Engineering, Beihang University, Beijing 100191, China.
** Corresponding author.
E-mail addresses: pangshujie@buaa.edu.cn (S.J. Pang), zhangtao@buaa.edu.cn (T. Zhang).

https://doi.org/10.1016/j.jallcom.2020.158436
0925-8388/

solutions [25–28]. This elemental segregation can be reduced by the heat treatment or laser surface melting, leading to the improvement in the corrosion resistance, while the alloys still suffered the pitting corrosion [29,30]. It has also been found that the minor addition of Ti into the Al–Cr–Fe–Co–Ni system HEAs increased the corrosion resistance of the alloys, but the addition of Ti with a high content would negatively impact the pitting-corrosion resistance of the alloys once intermetallic compounds formed [31–33]. For the Al–Cr–Fe–Co–Ni HEAs with the addition of Cu or Si, pitting corrosion in the NaCl solution also occurred [34,35]. Since high corrosion resistance besides good mechanical properties of the alloys are attractive for the practical long-term applications, it is of great significance to further improve the corrosion resistance of the Al–Cr–Fe–Co–Ni HEAs.

Among the Al–Cr–Fe–Co–Ni HEAs, the $Al_{0.3}CrFeCoNi$ alloy with FCC structure possesses a good ductility but a relatively-low strength [36,37]. Its strength can be improved by the increment of the BCC phase through increasing the Al content in the alloy [7–10], whereas the pitting-corrosion resistance in NaCl solutions was deteriorated [25–27]. On the other hand, it is known that Cr is a passivating element and a BCC-phase stabilizer [17,18,38]. In the present work, the effects of the Cr content on microstructure, corrosion behavior, and mechanical properties of $Al_{0.3}Cr_xFeCoNi$ (x = 0–2.0, in molar ratio) HEAs were systematically studied, and the HEAs with x = 1.5–2.0 possessing the improved corrosion resistance and good mechanical properties were successfully developed. The $Al_{0.3}Cr_xFeCoNi$ (x = 1.5–2.0) alloys consisting of the Cr-rich FCC and BCC phases exhibited excellent pitting-corrosion resistance in the 3.5 mass% NaCl solution. The related mechanisms are also discussed.

2. Experimental procedures

Alloy ingots with nominal compositions of $Al_{0.3}Cr_xFeCoNi$ (x = 0, 0.5, 1.0, 1.5, 1.7, and 2.0) were prepared by arc-melting the mixtures of the pure metals (purity > 99.99 mass%) in a Ti-gettered argon atmosphere. The ingots were remelted at least five times to ensure the chemical homogeneity. From the ingots, cylindrical samples with a dimension of ϕ 3 mm × 60 mm were produced by copper-mold casting in a high-purity argon atmosphere.

The microstructure of the $Al_{0.3}Cr_xFeCoNi$ alloys was examined by a D/MAX-2500 X-ray diffractometer (XRD), using the Cu-Kα radiation, a JXA-8100 scanning electron microscope (SEM) equipped with an energy disperse spectroscopy (EDS), and a JEM-2100 transmission electron microscope (TEM).

Corrosion behavior of the $Al_{0.3}Cr_xFeCoNi$ alloys was characterized by immersion tests and electrochemical measurements in a 3.5 mass % NaCl solution. Before the immersion, the surfaces of the slice specimens with a diameter of 3 mm and a thickness of 3 mm cut from the cast rods were polished with the SiC sandpaper up to 2000 grit, and then ultrasonically cleaned in the acetone and the deionized water, respectively. The ratio of the solution volume to the surface area was higher than 0.2 mL/mm^2, according to American Society for Testing and Materials (ASTM) standard G31–72 [39]. After the immersion in the NaCl solution for 30 days, the slice specimens were ultrasonically cleaned in the acetone and the deionized water, respectively. The surface and cross-section morphologies of the slice specimens before and after the immersion tests were observed, using a JSM 6010 SEM. The corrosion rates of the alloys were estimated according to the mass loss of the alloys, which were measured by the balance with a minimum digit of 0.01 mg, and the densities of the alloys measured by the Archimedes principle. Three specimens of each alloy were adopted to confirm reproducibility. For the electrochemical measurements, the specimens were mounted with epoxy, and the exposed transverse surfaces were polished with the SiC sandpaper up to 2000 grit, followed by the ultrasonically cleaning in the acetone and the deionized water, respectively. Then the samples were exposed to air for about 24 h in order to achieve good reproducibility. The electrochemical measurements were conducted, using an electrochemical workstation (EG&G Princeton Applied Research VersaSTAT III) and a standard three-electrode cell system, which consisted of a platinum foil as the counter electrode, a saturated calomel electrode (SCE) as the reference electrode, and a test specimen as the working electrode. After immersion in the solution for about 1800 s when the open-circuit potential (OCP) became almost steady, the potentiodynamic polarization was performed from the potential of 50 mV below the OCP at a scan rate of 50 mV/min. Measurements of the polarization curves were performed at least three times for reproducibility. The corrosion-current densities of the alloys were determined from the potentiodynamic-polarization curves, using the Tafel extrapolation method. The surface morphologies of the specimens before and after the potentiodynamic polarization were observed, using a JSM 6010 SEM. The electrochemical impedance spectroscopy (EIS) measurements were carried out at the OCP, using the applied alternating current (AC) signal with a voltage amplitude of 10 mV in the frequency range from 10^5 Hz to 10^{-2} Hz. The compositions of the surface films on the alloys were analyzed by ThermoFisher Scientific ESCALAB 250 XI X-ray photoelectron spectroscopy (XPS) employing the monochromatic Al-Kα radiation.

The tensile mechanical properties of the $Al_{0.3}Cr_xFeCoNi$ alloys were characterized by an INSTRON8801 machine with a strain rate of 2.0×10^{-4} s^{-1}. The rod-shaped samples with a gauge dimension of 1.8 mm in the diameter and 15 mm in the length machined from the cast rods were used for the tensile tests. An YYJ-10/10-L extensometer was employed to measure the strain of the samples during the tensile tests. The tensile fracture surfaces of the alloys were observed by a JSM 6010 SEM. The Vickers microhardness of the alloys was determined by an FM-800 Vickers microhardness tester under a constant load of 100 g for 15 s, and the average values of eleven tests on each alloy were used.

3. Results

3.1. Microstructural characterization

The X-ray diffraction (XRD) patterns of the $Al_{0.3}Cr_xFeCoNi$ alloys are shown in Fig. 1. The patterns of the alloys with Cr contents at x = 0–1.0 exhibit crystalline peaks corresponding to the FCC phase, and those for the alloys with higher Cr contents at x = 1.5–2.0 show the peaks of FCC and BCC phases, suggesting that a high Cr content

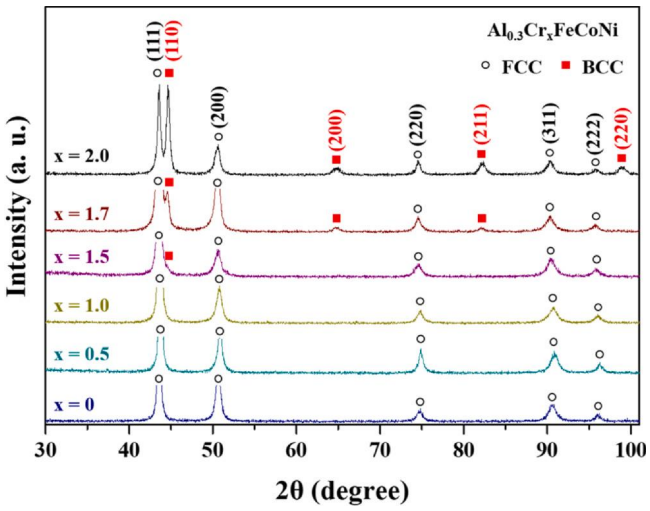

Fig. 1. X-ray diffraction patterns of the $Al_{0.3}Cr_xFeCoNi$ (x = 0–2.0) alloys.

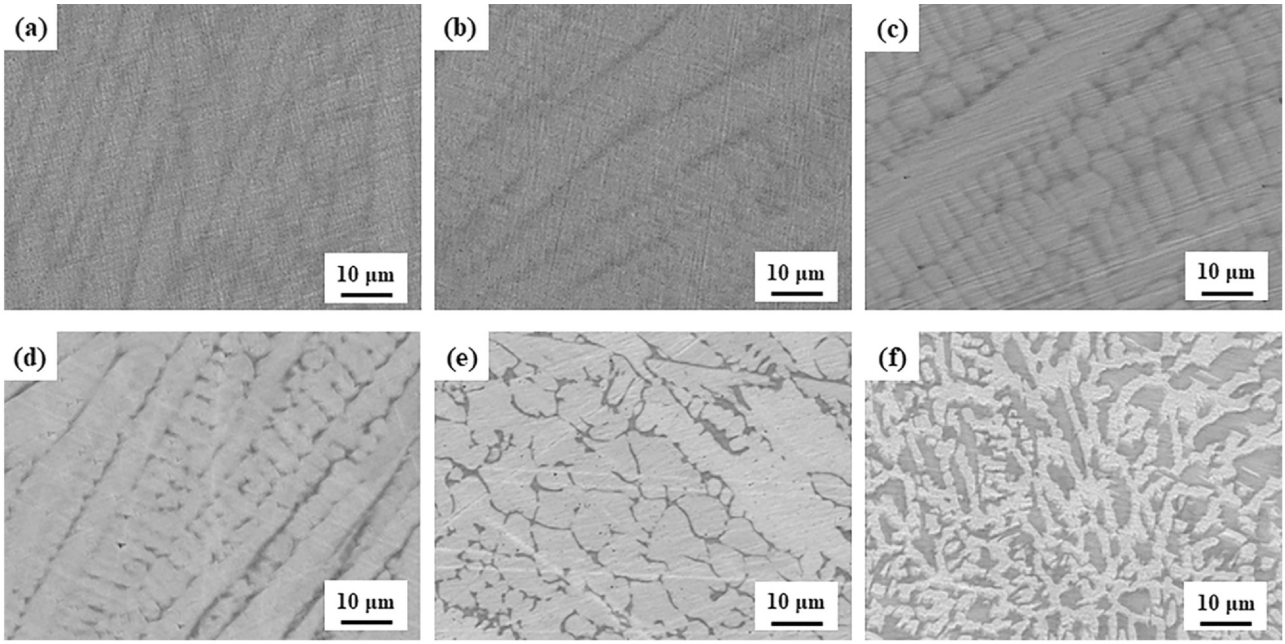

Fig. 2. SEM backscattering electron images of the $Al_{0.3}Cr_xFeCoNi$ alloys: (a) x = 0; (b) x = 0.5; (c) x = 1.0; (d) x = 1.5; (e) x = 1.7; (f) x = 2.0.

can facilitate the formation of the BCC phase in the $Al_{0.3}Cr_xFeCoNi$ alloys. The SEM backscattering electron images in Fig. 2 reveal that the $Al_{0.3}Cr_xFeCoNi$ alloys present the dendritic microstructure consisting of the bright dendritic region and the dark inter-dendritic region. The bright-field TEM images with insets of the selected area electron diffraction (SAED) patterns of the $Al_{0.3}Cr_xFeCoNi$ alloys shown in Fig. 3 confirm that the alloys with x = 0–1.0 possess the single FCC structure, and the alloys with x = 1.5–2.0 are composed of the duplex FCC + BCC structure with the ordered B2 nanoparticles uniformly distributed in the disordered BCC phase. These results suggest that the different contrast in the SEM images of the alloys with x = 0–1.0 is due to the heterogeneity of the elemental distribution in the FCC phase, and the bright dendritic region and the dark inter-dendritic region in the alloys with x = 1.5–2.0 correspond to the FCC phase and the BCC/B2 phases, respectively. With increasing the Cr content in the $Al_{0.3}Cr_xFeCoNi$ (x = 1.5–2.0) alloys, the inter-dendritic region is expanded, and the relative intensities of peaks for the BCC/B2 phases in the XRD patterns are enhanced, implying the increase in the amount of the BCC/B2 phases. The EDS-mapping images displayed in Fig. 4 reveal the distribution of each element in the $Al_{0.3}Cr_xFeCoNi$ alloys. The detailed chemical compositions of the dendritic and inter-dendritic regions characterized by the EDS point analyses are presented in Table 1. For the $Al_{0.3}Cr_xFeCoNi$ (x = 0–1.0) alloys with the single FCC structure, the Al and Ni contents in the inter-dendritic region are higher than those in the dendritic region, while the Fe and Co contents in the inter-dendritic region are lower than those in the dendritic region. The Cr contents in the inter-dendritic region of the alloys with x = 0.5 and 1.0 are slightly higher than those in the dendritic region. For the $Al_{0.3}Cr_xFeCoNi$ (x = 1.5–2.0) alloys with the FCC + BCC/B2 structure, the contents of Fe, Co, and Ni in the BCC/B2 phases are slightly lower than those in the FCC phases, and the contents of Al and Cr in the BCC/B2 phases are higher than those in the FCC phase, which are different from those for the Al–Cr–Fe–Co–Ni HEAs with the deficiency of Cr in the BCC phase [25–28]. It is notable that, for the $Al_{0.3}Cr_xFeCoNi$ alloys at x = 1.5–2.0, both the FCC and the BCC/B2 phases contain high-concentration Cr of over 30 atomic percent (at%), which is much higher than those of the other constituent elements. The present $Al_{0.3}Cr_xFeCoNi$ (x = 1.5–2.0) alloys consisting of these Cr-rich FCC and BCC/B2 phases may present improvement in the corrosion behavior.

3.2. Corrosion behavior

Surface morphologies of the $Al_{0.3}Cr_xFeCoNi$ alloys after the immersion in the 3.5 mass% NaCl solution for 30 days are shown in Fig. 5. The Cr-free $Al_{0.3}FeCoNi$ alloy after the immersion exhibits a localized-corrosion morphology on the surface, and its corrosion rate was estimated to be about 7.8×10^{-3} mm/year by the mass loss. After the immersion, the Cr-containing alloys demonstrate no change in the polished appearance, and no mass loss was detected, which implies their corrosion rates of less than 10^{-3} mm/year. The cross-section of the Cr-free $Al_{0.3}FeCoNi$ alloy also displayed localized corrosion, whereas the Cr-containing $Al_{0.3}Cr_xFeCoNi$ alloys showed the surfaces without corrosion in their cross-section. These results indicate that the corrosion resistance of the Cr-containing $Al_{0.3}Cr_xFeCoNi$ alloys is higher than that of the Cr-free $Al_{0.3}FeCoNi$ alloy.

The potentiodynamic-polarization curves of the $Al_{0.3}Cr_xFeCoNi$ alloys in the 3.5 mass% NaCl solution are plotted in Fig. 6, and the derived values of corrosion parameters are presented in Table 2. It can be seen that the alloys are spontaneously passivated with the passive current densities around 10^{-1} A/m^2. The fluctuations of the current density in the passive regions may correspond to the processes of the breakdown and repair of the passive films [40,41]. The alloys with low Cr contents at x = 0–1.0 suffer pitting corrosion when the anodic potential ascends to the potential in the range of about 0.104–0.535 V, and the pitting potential increases with increasing the Cr content in the alloys. It is notable that the alloys with higher Cr contents at x = 1.5–2.0 exhibit no pitting by the anodic polarization up to 2 V. After the potentiodynamic polarization, the $Al_{0.3}Cr_xFeCoNi$ (x = 0–1.0) alloys showed the pits on the surfaces, while the $Al_{0.3}Cr_xFeCoNi$ (x = 1.5–2.0) alloys exhibited no change in the surface morphologies. These results indicate that the present alloys with the Cr-rich FCC and BCC/B2 phases possess excellent pitting-corrosion resistance in the NaCl solution. Moreover, the increase in the Cr content from x = 0 to 2.0 leads to the decrease in the corrosion-current density from ~ 5.0×10^{-3} A/m^2 to ~ 1.4×10^{-4} A/m^2,

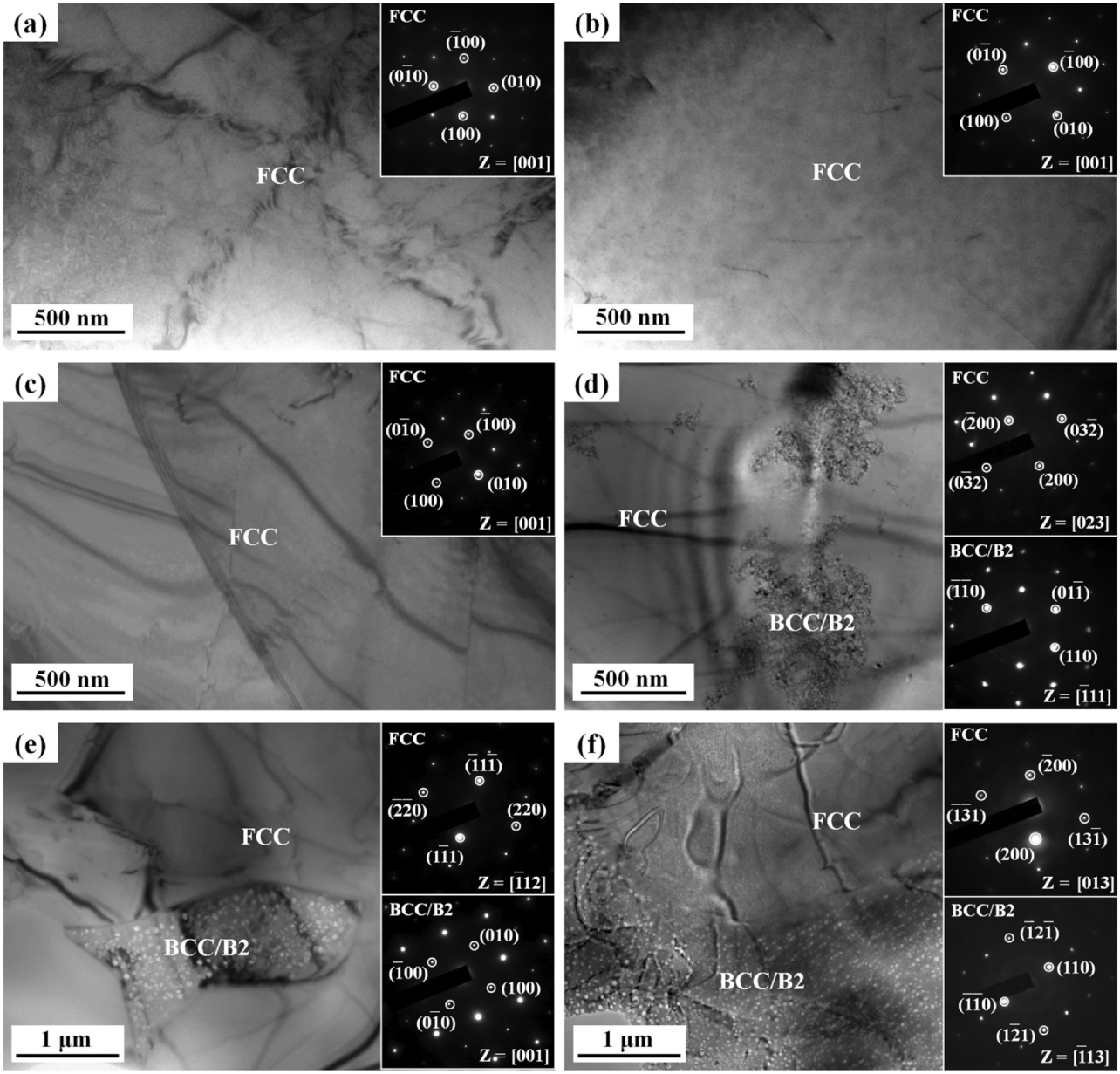

Fig. 3. Bright-field TEM images with insets of the selected area electron diffraction (SAED) patterns of the $Al_{0.3}Cr_xFeCoNi$ alloys: (a) x = 0; (b) x = 0.5; (c) x = 1.0; (d) x = 1.5; (e) x = 1.7; (f) x = 2.0.

and the increase in the corrosion potential from ~ −0.204 V to ~ −0.099 V, as listed in Table 2. These results indicate that the corrosion resistance of the $Al_{0.3}Cr_xFeCoNi$ alloys is effectively enhanced by increasing the Cr content.

Nyquist and Bode plots of the $Al_{0.3}Cr_xFeCoNi$ alloys in the 3.5 mass% NaCl solution at the open circuit potential are shown in Fig. 7. The radii of the semicircle arcs in the Nyquist plots are enlarged with increasing the Cr content, suggesting the enhancement of the impedance of the passive films on the alloys. This trend indicates the improvement in corrosion resistance with the increase in the Cr content of the $Al_{0.3}Cr_xFeCoNi$ alloys, which is in agreement with the results of the immersion tests and the potentiodynamic polarization. In the Bode plots, a linear relationship with a slope below −1 between the logarithms of the impedance modulus and the logarithms of the frequencies is obtained in the medium-frequency range, and the phase angle achieves a maximum value of about 75–85°. These results indicate a capacitive response related to the presence of barrier passive films. The $R_s(R_{ct}Q)$ model [42] displayed in Fig. 7c is used to fit the impedance spectra of the present alloys, where R_s denotes the solution resistance, R_{ct} represents the charge transfer resistance, which reflects the corrosion rate of a metal in solutions, and Q denotes the constant phase element (CPE) instead of the pure capacity in consideration of inhomogeneous surfaces and adsorption effects. The CPE impedance (Z_{CPE}) is defined by

$$Z_{CPE} = Y_0^{-1}(j\omega)^{-n} \quad (1)$$

where Y_0 is the proportionality factor, j is the imaginary unit, ω is the angular frequency, and n is the dispersion coefficient varying from −1 to 1 [42]. The CPE corresponds to a capacitor for $n = 1$, to a resistor for $n = 0$, and to an inductance for $n = -1$ [42]. The values of the equivalent circuit parameters are summarized in Table 3. It is seen that the R_{ct} value increases with increasing the Cr content, and the high R_{ct} values of the alloys with Cr contents at x = 1.5–2.0 imply their high corrosion resistance. This result is consistent with the potentiodynamic-polarization curves, showing the large passive

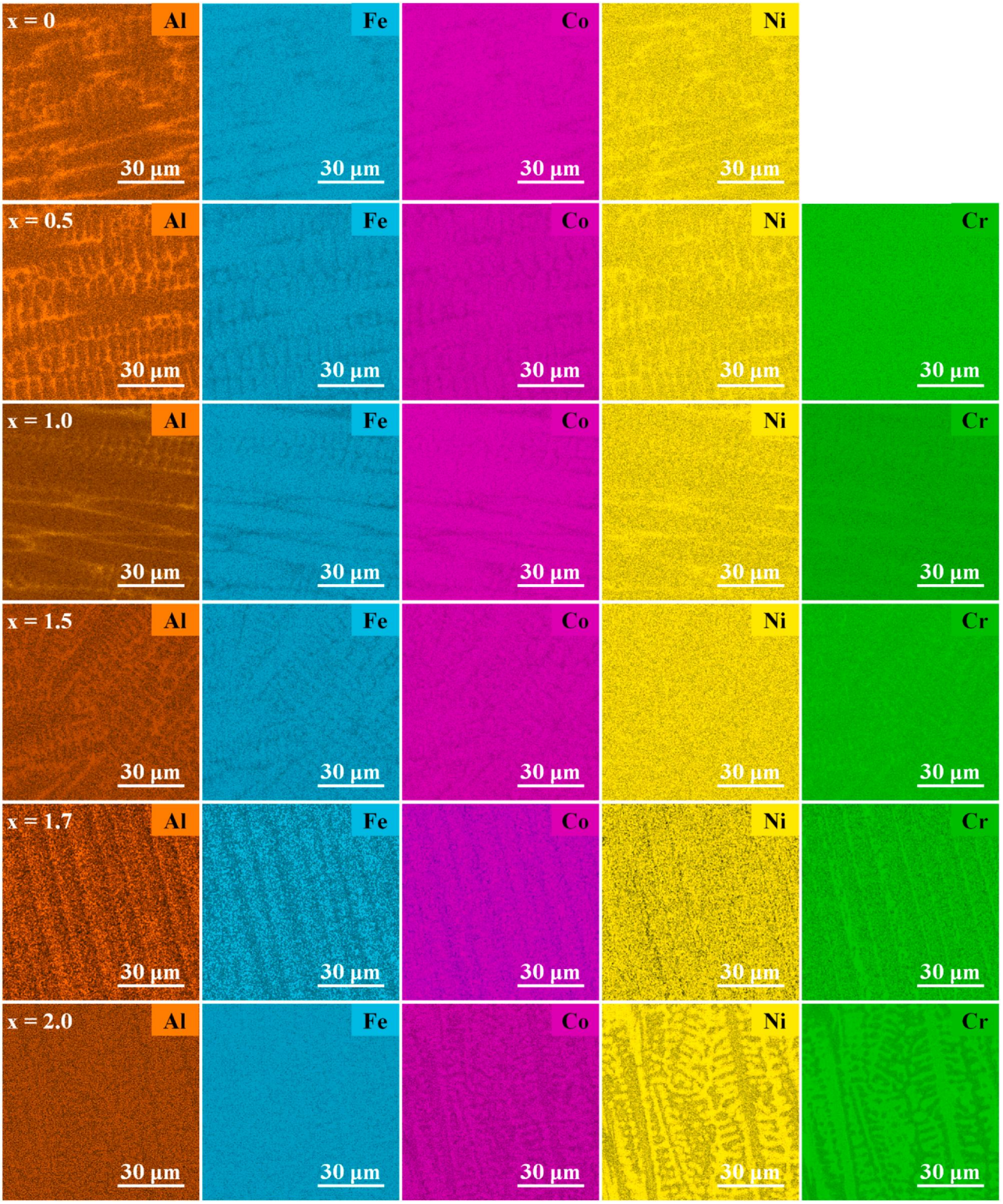

Fig. 4. EDS-mapping images of the $Al_{0.3}Cr_xFeCoNi$ (x = 0–2.0) alloys.

regions and excellent pitting-corrosion resistance of the alloys with Cr contents at x = 1.5–2.0.

The chemical compositions of the air-formed surface films on the $Al_{0.3}Cr_xFeCoNi$ (x = 0–2.0) alloys were analyzed by XPS. The spectra of Al 2p, Cr $2p_{3/2}$, Fe $2p_{3/2}$, Co $2p_{3/2}$, and Ni $2p_{3/2}$ are presented in Fig. 8a–e. As shown in Fig. 8a, the Al 2p spectra for the alloys are separated into two peaks corresponding to Al_2O_3 (Al^{3+}) in an oxide state and Al (Al^0) in the metallic state, respectively. The de-convoluted Cr $2p_{3/2}$ spectra in Fig. 8b reveal the presence of Cr_2O_3 (Cr^{3+}) and the metallic Cr (Cr^0) in the surface films of the alloys with x = 0.5–2.0. In Fig. 8c, the spectra for the Fe $2p_{3/2}$ show three peaks corresponding to Fe_2O_3 (Fe^{3+}), FeO (Fe^{2+}), and Fe (Fe^0). The peaks of CoO (Co^{2+}) and Co (Co^0) are seen in the Co $2p_{3/2}$ spectra in Fig. 8d. Similarly, the peaks of NiO (Ni^{2+}) and Ni (Ni^0) are detected in the Ni

Table 1
Chemical compositions of the dendritic region (DR) and the inter-dendritic region (ID) in the $Al_{0.3}Cr_xFeCoNi$ (x = 0–2.0) alloys determined by EDS.

Alloy	Region	Al (at%)	Cr (at%)	Fe (at%)	Co (at%)	Ni (at%)
x = 0	DR	7.3 ± 0.3	–	31.5 ± 0.2	31.3 ± 0.3	28.9 ± 0.2
	ID	9.7 ± 0.6	–	29.2 ± 0.3	29.0 ± 0.6	32.1 ± 0.3
x = 0.5	DR	6.3 ± 0.2	13.1 ± 0.1	27.5 ± 0.2	27.1 ± 0.1	25.9 ± 0.1
	ID	9.4 ± 0.2	13.5 ± 0.1	24.3 ± 0.2	24.3 ± 0.1	28.5 ± 0.2
x = 1.0	DR	5.6 ± 0.1	23.2 ± 0.1	24.2 ± 0.1	24.1 ± 0.2	23.0 ± 0.1
	ID	8.3 ± 0.6	24.0 ± 0.3	21.2 ± 0.9	21.7 ± 0.8	24.8 ± 0.8
x = 1.5	DR	4.8 ± 0.1	31.1 ± 0.2	21.9 ± 0.1	21.6 ± 0.3	20.7 ± 0.4
	ID	8.0 ± 0.4	37.8 ± 0.8	17.9 ± 0.2	17.5 ± 0.4	18.9 ± 0.8
x = 1.7	DR	4.8 ± 0.2	33.8 ± 0.2	20.8 ± 0.3	20.5 ± 0.3	20.1 ± 0.3
	ID	6.9 ± 0.1	40.8 ± 0.9	18.2 ± 0.3	17.5 ± 0.3	16.7 ± 0.4
x = 2.0	DR	5.1 ± 0.2	33.9 ± 0.2	19.6 ± 0.2	19.7 ± 0.2	21.7 ± 0.2
	ID	6.0 ± 0.2	41.7 ± 0.4	18.8 ± 0.1	17.3 ± 0.2	16.3 ± 0.2

$2p_{3/2}$ spectra in Fig. 8e. The cationic fractions in the surface films and the nominal contents of the constituent elements for the $Al_{0.3}Cr_xFeCoNi$ (x = 0–2.0) alloys are presented in Fig. 8f. For the Cr-free $Al_{0.3}FeCoNi$ alloy, compared with the nominal composition of the alloy, the surface film contains higher contents of Al, Co, and Ni and a lower content of Fe. For the Cr-containing $Al_{0.3}Cr_xFeCoNi$ (x = 0.5–2.0) alloys, the surface films are enriched in Al and Cr cations and deficient in Co and Ni cations in comparison with the nominal compositions of the alloys. The Fe contents in the surface films of the alloys with x = 0.5–2.0 are similar to the nominal Fe contents in the alloys. The XPS results indicate that the content of Cr_2O_3 in the surface films increases with the addition of Cr, contributing to the improvement in the corrosion resistance of the alloys.

3.3. Mechanical properties

The engineering tensile stress–strain curves of the $Al_{0.3}Cr_xFeCoNi$ alloys are presented in Fig. 9, from which the tensile yield strength

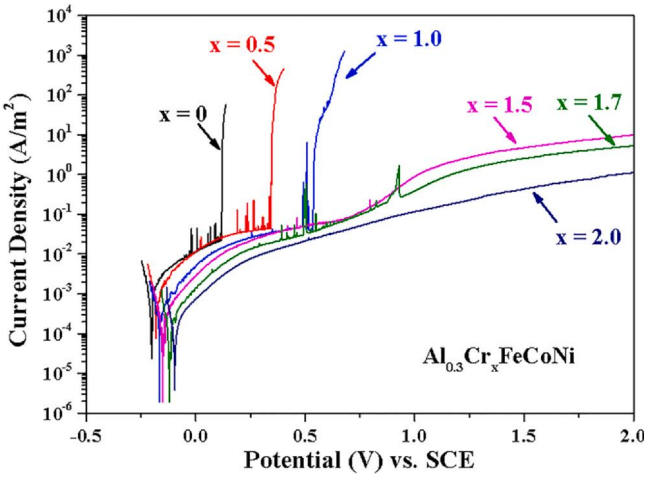

Fig. 6. Potentiodynamic-polarization curves of the $Al_{0.3}Cr_xFeCoNi$ (x = 0–2.0) alloys in the 3.5 mass% NaCl solution.

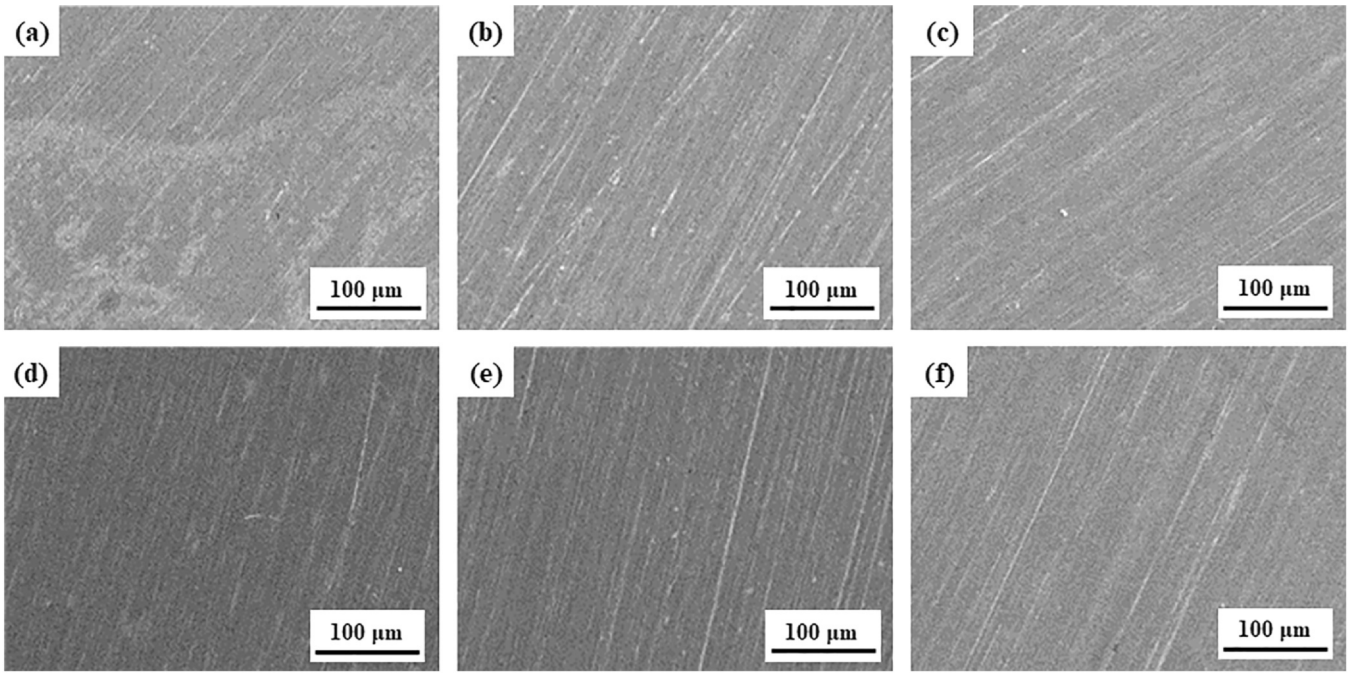

Fig. 5. SEM images of the surfaces of the $Al_{0.3}Cr_xFeCoNi$ alloys after immersion in the 3.5 mass% NaCl solution for 30 days: (a) x = 0; (b) x = 0.5; (c) x = 1.0; (d) x = 1.5; (e) x = 1.7; (f) x = 2.0.

Table 2
Electrochemical parameters of the $Al_{0.3}Cr_xFeCoNi$ (x = 0–2.0) alloys in the 3.5 mass% NaCl solution.

Alloy	E_{corr} (V)	i_{corr} ($\times 10^{-3}$ A/m^2)	E_{pit} (V)
x = 0	−0.204 ± 0.012	5.02 ± 0.55	0.104 ± 0.013
x = 0.5	−0.185 ± 0.010	1.01 ± 0.14	0.350 ± 0.015
x = 1.0	−0.155 ± 0.008	0.77 ± 0.06	0.535 ± 0.030
x = 1.5	−0.149 ± 0.006	0.57 ± 0.14	–
x = 1.7	−0.129 ± 0.009	0.30 ± 0.05	–
x = 2.0	−0.099 ± 0.011	0.14 ± 0.04	–

(σ_y), tensile strength (σ_{UTS}), and elongation to fracture (δ) can be measured, and their values are listed in Table 4. It is seen that the strengths of the alloys increased with increasing the Cr content. The alloys at x = 0–1.0 exhibit tensile yield strengths of 221–259 MPa, tensile strengths of 486–559 MPa, and large elongations of over 40%. The alloy with a higher Cr content of x = 1.5 displays an improved tensile yield strength (294 MPa) and tensile strength (640 MPa), and keeps a large tensile elongation of about 40%. The σ_y and σ_{UTS} are further enhanced to 338 MPa and 742 MPa with increasing the Cr content to x = 1.7, and then drastically up to 546 MPa and 1078 MPa at x = 2.0, respectively, accompanied by the reduction of the elongation due to the increased amount of the BCC/B2 phases in the alloys. Moreover, obvious serrations are observed on the stress–-strain curve of the alloy with x = 2.0, which contains a relatively-large amount of the B2 nanoparticles in comparison with the other alloys with x = 0–1.7. The tensile fracture surfaces of the alloys exhibit abundant dimples (Fig. 10), which are typical of the ductile fracture. In addition, the Vickers microhardness of the $Al_{0.3}Cr_xFeCoNi$ alloys is increased from ~ 153 Hv to ~ 343 Hv as the Cr content increases from x = 0–2.0, indicating that the increased BCC/B2 phases significantly harden the alloys.

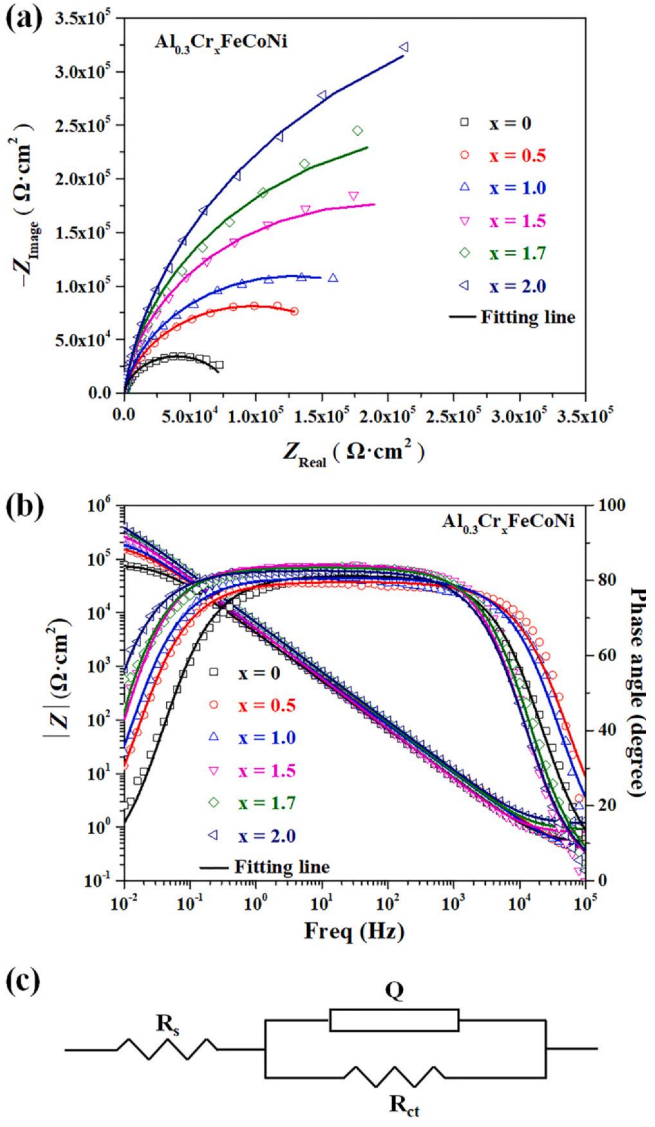

Fig. 7. (a) Nyquist plots, (b) Bode plots, and (c) equivalent electrical circuit for fitting the EIS data of the $Al_{0.3}Cr_xFeCoNi$ (x = 0–2.0) alloys at the open circuit potential in the 3.5 mass% NaCl solution.

4. Discussion

Microstructural characterization indicated that the $Al_{0.3}Cr_xFeCoNi$ alloys with x = 0–1.0 exhibited the single FCC structure. The alloys with x = 1.5–2.0 consisted of the FCC + BCC/B2 structure, and the amount of the BCC/B2 phases increased with increasing the Cr content in the alloys. It has been proposed that the stability of the FCC and BCC solid solutions in HEAs can be delineated by the valence electron concentration (VEC) of HEAs [43]. The VEC was defined as the weighted average from the VEC of the constituent components, i. e.,

$$VEC = \sum_{i=0}^{n} c_i(VEC)_i \quad (2)$$

where c_i is the atomic percentage of the i-th element, and $(VEC)_i$ is its valence electron concentration [43]. For a specific HEA system, the FCC phase is stable at a higher VEC, while the BCC phase is stable at a lower VEC [43]. The VEC values of Al, Cr, Fe, Co, and Ni are 3, 6, 8, 9, and 10, respectively [44]. Therefore, the increase in the Cr content of the $Al_{0.3}Cr_xFeCoNi$ alloys resulted in a decrease in the VEC values of the alloys. The decrease in the VEC values of the present alloys implies the improvement in the stability of the BCC phase [10,15,43], which is in agreement with the effect of Cr on facilitating the formation of the BCC phase in the alloys. Moreover, the Cr content in the BCC/B2 and the FCC phases in the alloys with x = 1.5–2.0 was increased with increasing the Cr content of the alloys. The high Cr contents of the $Al_{0.3}Cr_xFeCoNi$ (x = 1.5–2.0) alloys resulted in the formation of the Cr-rich BCC/B2 and FCC phases, which could be crucial to the improved corrosion resistance of the alloys.

The results of the immersion, potentiodynamic polarization, and EIS indicated the enhancement of the corrosion resistance of the $Al_{0.3}Cr_xFeCoNi$ alloys with increasing the Cr content in the 3.5 mass% NaCl solution. Cr is known as a passivating element that can improve the protectiveness of surface films of alloys, leading to the enhancement of the corrosion resistance [38]. For the $Al_{0.3}Cr_xFeCoNi$ (x = 0–1.0) alloys with the single FCC structure, the pitting potential increased with increasing the Cr content. The improved corrosion resistance is attributed to the increase of Cr_2O_3 in the surface films [38]. With the further addition of Cr to x = 1.5–2.0, the alloys with the FCC + BCC/B2 structure exhibited higher Cr contents in the constituent phases, which is favorable for the enhancement of the corrosion resistance of the alloys. It has been reported that $Al_xCrFeCoNi$ alloys with duplex FCC + BCC structure tended to suffer pitting corrosion at the BCC phase due to the deficiency of Cr in the BCC phase [25–29]. By contrast, for the present $Al_{0.3}Cr_xFeCoNi$ (x = 1.5–2.0) alloys, the concentrations of Cr in both the BCC/B2 and the FCC phases reach over 30 at% and are much higher than those of the other constituent elements, which could lead to the avoidance of pitting corrosion induced by the deficiency of Cr in the BCC phase. The XPS

Table 3
Values of electrical equivalent circuit (EEC) parameters of the $Al_{0.3}Cr_xFeCoNi$ (x = 0–2.0) alloys in the 3.5 mass% NaCl solution.

Alloy	R_s (Ω cm^2)	Y_0 (s^n Ω^{-1} cm^{-2})	n	R_{ct} (Ω cm^2)	$\sum\chi^2$
x = 0	16.18	1.39×10^{-6}	0.90	2.55×10^{3}	2.20×10^{-3}
x = 0.5	9.93	1.26×10^{-6}	0.89	6.21×10^{3}	3.68×10^{-3}
x = 1.0	11.72	1.22×10^{-6}	0.90	8.19×10^{3}	3.13×10^{-3}
x = 1.5	25.32	1.11×10^{-6}	0.94	1.24×10^{4}	4.26×10^{-3}
x = 1.7	28.66	8.83×10^{-7}	0.93	1.74×10^{4}	1.87×10^{-3}
x = 2.0	37.13	8.81×10^{-7}	0.92	2.67×10^{4}	1.18×10^{-3}

results further revealed that on the surfaces of the alloys consisting of these Cr-rich FCC and BCC/B2 phases, the surface films enriched in Cr_2O_3 were formed (Fig. 8), leading to the high corrosion resistance in the NaCl solution.

Fig. 11 shows the corrosion-current densities and pitting potentials of the present $Al_{0.3}Cr_xFeCoNi$ alloys in comparison with those of the $Al_xCrFeCoNi$ [25,28,29,45] in as-cast, hot-isostatic-pressing (HIP) treated, forged, or homogenized states, CoCrFeMnNi

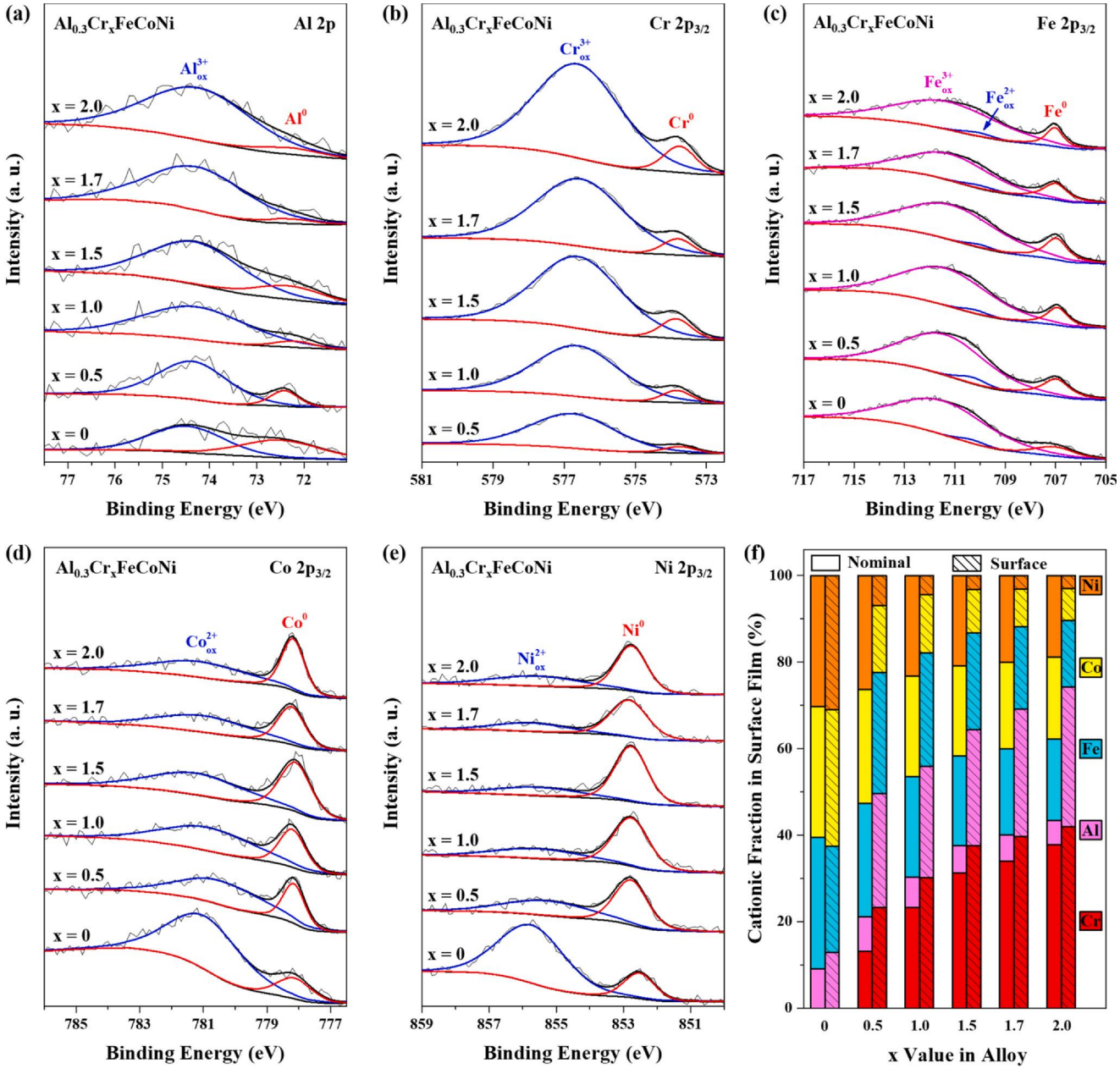

Fig. 8. XPS spectra of (a) Al 2p, (b) Cr $2p_{3/2}$, (c) Fe $2p_{3/2}$, (d) Co $2p_{3/2}$, and (e) Ni $2p_{3/2}$ as well as (f) cationic fractions in the air-formed surface films and the nominal contents of the constituent elements for the $Al_{0.3}Cr_xFeCoNi$ (x = 0–2.0) alloys.

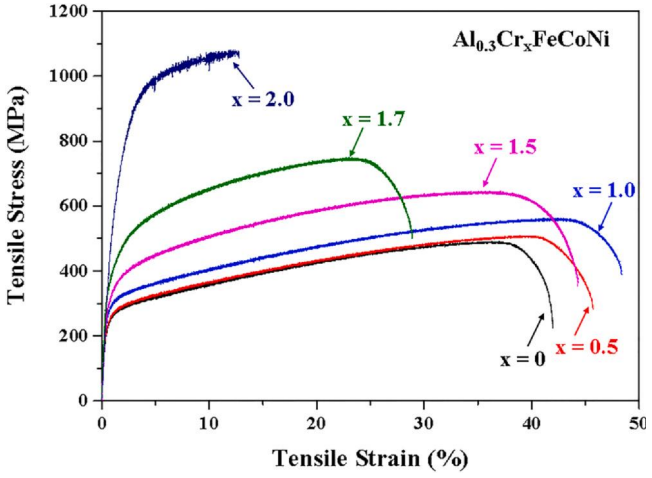

Fig. 9. Tensile stress–strain curves of the $Al_{0.3}Cr_xFeCoNi$ (x = 0–2.0) alloys.

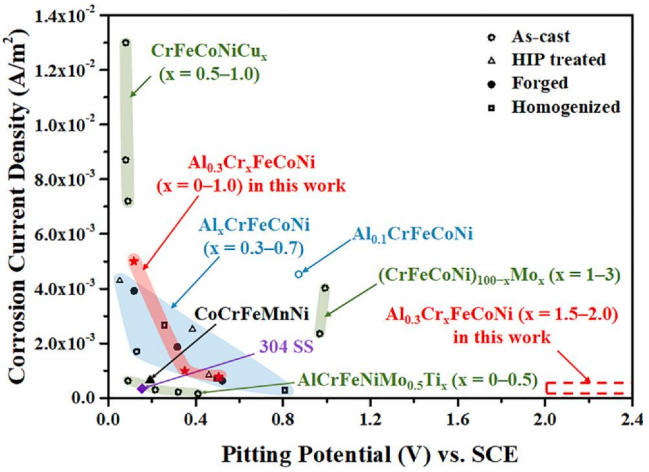

Fig. 11. Corrosion-current densities and pitting potentials of the $Al_{0.3}Cr_xFeCoNi$ (x = 0–2.0) alloys in comparison with those of the reported HEAs and 304 stainless steel (SS) in the 3.5 mass% NaCl solution [25,28,29,45–52].

Table 4
Tensile yield strength (σ_y), tensile strength (σ_{UTS}), elongation to fracture (δ), and Vickers microhardness (Hv) for the $Al_{0.3}Cr_xFeCoNi$ (x = 0–2.0) alloys.

Alloy	σ_y (MPa)	σ_{UTS} (MPa)	δ (%)	Hv
x = 0	221	486	41	153 ± 4
x = 0.5	233	504	45	163 ± 9
x = 1.0	259	559	47	171 ± 2
x = 1.5	294	640	44	191 ± 6
x = 1.7	338	742	28	229 ± 9
x = 2.0	546	1078	11	343 ± 10

[46], $AlCrFeNiMo_{0.5}Ti_x$ [47], $CrFeCoNiCu_x$ [48–50], and $(CrFeCoNi)_{100-x}Mo_x$ [51] HEAs, and the 304 stainless steel [52] in the 3.5 mass% NaCl solution. For the $Al_{0.3}Cr_xFeCoNi$ (x = 1.5–2.0) alloys studied in the present work, the rectangle region with the dashed border and without the right boundary is adopted in the figure to delimit the approximate scope of pitting potentials, since no pitting occurred under the anodic polarization up to 2 V vs. SCE. Compared with the 304 stainless steel and the other HEAs, including the $Al_xCrFeCoNi$ HEAs with improved corrosion resistance achieved by homogenization, the $Al_{0.3}Cr_xFeCoNi$ (x = 1.5–2.0) alloys exhibit low corrosion-current densities and higher pitting-corrosion potential, suggesting that the present alloys possess high corrosion resistance. It is further demonstrated that increasing the Cr content in Al–Cr–Fe–Co–Ni alloys is an effective way for tailoring corrosion-resistant alloys.

The compositional and microstructural variations of the $Al_{0.3}Cr_xFeCoNi$ alloys also induced the changes in the mechanical properties of the alloys. It was indicated that the $Al_{0.3}Cr_xFeCoNi$ (x = 0–1.0) alloys exhibited the relatively-low tensile strength and hardness and large tensile elongation attributed to the single FCC structure. With the further increase of the Cr content, the alloys with x = 1.5–2.0 exhibited the improved tensile strength and hardness. It has been reported that in the Al–Cr–Fe–Co–Ni HEAs, the strength and hardness of the BCC phase are higher than those of the FCC phase [7,18], and the uniformly-distributed B2 nanoparticles in the BCC

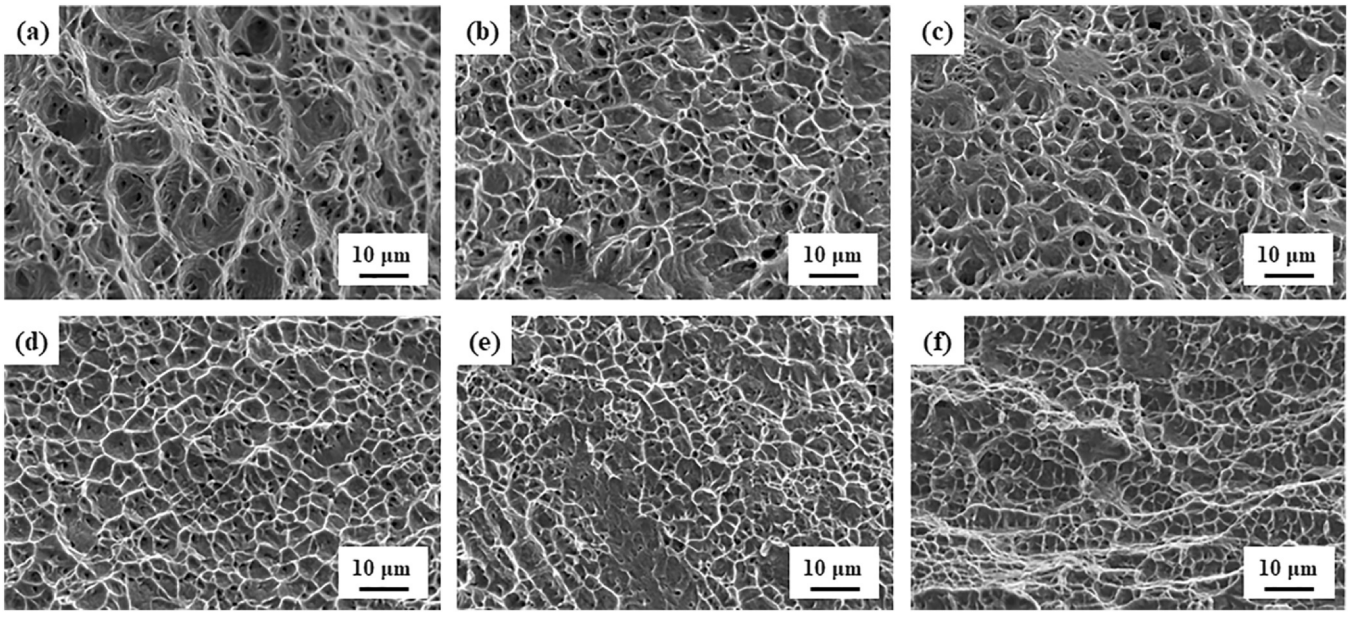

Fig. 10. SEM images of the tensile fracture surfaces of the $Al_{0.3}Cr_xFeCoNi$ alloys: (a) x = 0; (b) x = 0.5; (c) x = 1.0; (d) x = 1.5; (e) x = 1.7; (f) x = 2.0.

phase can enhance the strength and hardness of alloys due to the precipitation-strengthening effect [11,19,22]. The alloy with x = 1.5 containing the small amount of BCC/B2 phases maintained the large tensile elongation. For the alloys (x = 1.7 and 2.0) with the increased BCC/B2 phases, the tensile elongation was reduced, since the BCC phases possess less operable slip systems in comparison with the FCC phases. Additionally, the stress–strain curve of the alloy with x = 2.0 exhibited obvious serrations, which could be related to the pinning and unpinning of dislocations induced by the B2 nanoparticles with a relatively-large amount during deformation [53,54]. It is notable that the $Al_{0.3}Cr_xFeCoNi$ (x = 1.5–2.0) alloys with high corrosion resistance exhibited good mechanical properties, including the tensile strengths of 640–1078 MPa, and tensile elongations of 11–44%.

5. Conclusions

In this study, the effects of the Cr content on the microstructure, corrosion behavior, and mechanical properties of the $Al_{0.3}Cr_xFeCoNi$ (x = 0–2.0) alloys were investigated. The $Al_{0.3}Cr_xFeCoNi$ (x = 1.5–2.0) alloys with high corrosion resistance and good mechanical properties were developed. The following conclusions are drawn.

(1) The $Al_{0.3}Cr_xFeCoNi$ alloys with x = 0–1.0 exhibited the single FCC structure. The alloys with x = 1.5–2.0 consisted of FCC + BCC/B2 structure, and the amount of the BCC/B2 phases increased with increasing the Cr content in the alloys. The addition of Cr also resulted in the increase of the Cr concentration in both the FCC and BCC/B2 phases, and the Cr-rich FCC and BCC/B2 phases were formed in the alloys with Cr contents at x = 1.5–2.0.

(2) The Cr-containing $Al_{0.3}Cr_xFeCoNi$ alloys exhibited corrosion rates less than 10^{-3} mm/year in the 3.5 mass% NaCl solution, lower than that of the $Al_{0.3}FeCoNi$ alloy. The alloys were spontaneously passivated in the NaCl solution, and the increase in the Cr content from x = 0 to 2.0 caused the decrease in the corrosion-current density and the improvement in the corrosion potential, pitting-corrosion resistance, and charge-transfer resistance. The $Al_{0.3}Cr_xFeCoNi$ (x = 1.5–2.0) alloys consisting of the Cr-rich FCC and BCC/B2 phases exhibited high corrosion resistance, and no pitting occurred under the anodic polarization up to 2 V vs. SCE in the NaCl solution, which could be attributed to the formation of the protective surface films enriched in Cr_2O_3.

(3) The $Al_{0.3}Cr_xFeCoNi$ (x = 0–1.0) alloys with the FCC structure exhibited the relatively-low tensile strength (486–559 MPa) and large tensile elongation (> 40%). The further addition of Cr in the alloys leads to the enhancement of the tensile strength and hardness due to the increased amount of the BCC/B2 phases. The $Al_{0.3}Cr_xFeCoNi$ (x = 1.5–2.0) alloys with the high corrosion resistance possess tensile strengths of 640–1078 MPa and tensile elongations of 11–44%, indicating their good mechanical properties.

CRediT authorship contribution statement

Xiaolei Yan: Methodology, Investigation, Data curation, Writing - original draft. **Hui Guo:** Methodology, Investigation, Data curation. **Wei Yang:** Methodology, Writing - review & editing. **Shujie Pang:** Conceptualization, Methodology, Supervision, Writing - review & editing, Resources, Funding acquisition. **Qing Wang:** Writing - review & editing. **Ying Liu:** Writing - review & editing. **Peter K. Liaw:** Writing - review & editing. **Tao Zhang:** Resources, Supervision.

Declaration of competing interest

The authors declare that they have no known competing financial interests or personal relationships that could have appeared to influence the work reported in this paper.

Acknowledgement

This work was financially supported by National Natural Science Foundation of China (Grant No. 51971007) and the 111 Project (Grant No. B17002). PKL very much appreciates the supports from the National Science Foundation (DMR-1611180 and 1809640) with the program directors, Drs. Judith Yang, Gary Shiflet, and Diana Farkas.

References

[1] J.W. Yeh, S.K. Chen, S.J. Lin, J.Y. Gan, T.S. Chin, T.T. Shun, C.H. Tsau, S.Y. Chang, Nanostructured high-entropy alloys with multiple principal elements: novel alloy design concepts and outcomes, Adv. Eng. Mater. 6 (2004) 299–303.
[2] B. Cantor, I.T.H. Chang, P. Knight, A.J.B. Vincent, Microstructural development in equiatomic multicomponent alloys, Mater. Sci. Eng. A 375 (2004) 213–218.
[3] E.P. George, W.A. Curtin, C.C. Tasan, High entropy alloys: a focused review of mechanical properties and deformation mechanisms, Acta Mater. 188 (2020) 435–474.
[4] D.B. Miracle, O.N. Senkov, A critical review of high entropy alloys and related concepts, Acta Mater. 122 (2017) 448–511.
[5] Y. Zhang, T.T. Zuo, Z. Tang, M.C. Gao, K.A. Dahmen, P.K. Liaw, Z.P. Lu, Microstructures and properties of high-entropy alloys, Prog. Mater. Sci. 61 (2014) 1–93.
[6] Y. Dong, Z.Q. Yao, X. Huang, F.M. Du, C.Q. Li, A.F. Chen, F. Wu, Y.Q. Cheng, Z.R. Zhang, Microstructure and mechanical properties of $AlCo_xCrFeNi_{3-x}$ eutectic high-entropy-alloy system, J. Alloys Compd. 823 (2020) 153886.
[7] W.R. Wang, W.L. Wang, S.C. Wang, Y.C. Tsai, C.H. Lai, J.W. Yeh, Effects of Al addition on the microstructure and mechanical property of $Al_xCoCrFeNi$ high-entropy alloys, Intermetallics 26 (2012) 44–51.
[8] W.R. Wang, W.L. Wang, J.W. Yeh, Phases, microstructure and mechanical properties of $Al_xCoCrFeNi$ high-entropy alloys at elevated temperatures, J. Alloys Compd. 589 (2014) 143–152.
[9] A. Sourav, S. Yebaji, S. Thangaraju, Structure-property relationships in hot forged $Al_xCoCrFeNi$ high entropy alloys, Mater. Sci. Eng. A 793 (2020) 139877.
[10] S.G. Yang, J. Lu, F.Z. Xing, L.J. Zhang, Y. Zhong, Revisit the VEC rule in high entropy alloys (HEAs) with high-throughput CALPHAD approach and its applications for material design-a case study with Al–Co–Cr–Fe–Ni system, Acta Mater. 192 (2020) 11–19.
[11] Y. Ma, Q. Wang, B.B. Jiang, C.L. Li, J.M. Hao, X.N. Li, C. Dong, T.G. Nieh, Controlled formation of coherent cuboidal nanoprecipitates in body-centered cubic high-entropy alloys based on $Al_2(Ni,Co,Fe,Cr)_{14}$ compositions, Acta Mater. 147 (2018) 213–225.
[12] M. Liu, W.Y. Xu, S.D. Zhang, Z.M. Wang, Z.Y. Wang, B.J. Wang, D. Wang, F.J. Li, Microstructures and hardnesses of $AlCoCr_{0.5}Fe_xNi_{2.5}$ high entropy alloys with equal valence electron concentration, J. Alloys Compd. 824 (2020) 153881.
[13] L. Guo, D.H. Xiao, W.Q. Wu, S. Ni, M. Song, Effect of Fe on microstructure, phase evolution and mechanical properties of $(AlCoCrFeNi)_{100-x}Fe_x$ high entropy alloys processed by spark plasma sintering, Intermetallics 103 (2018) 1–11.
[14] M.J. Kang, K.R. Lim, J.W. Won, Y.S. Na, Effect of Co content on the mechanical properties of A2 and B2 phases in $AlCo_xCrFeNi$ high-entropy alloys, J. Alloys Compd. 769 (2018) 808–812.
[15] R.R. Chen, G. Qin, H.T. Zheng, L. Wang, Y.Q. Su, Y.L. Chiu, H.S. Ding, J.J. Guo, H.Z. Fu, Composition design of high entropy alloys using the valence electron concentration to balance strength and ductility, Acta Mater. 144 (2018) 129–137.
[16] Y.P. Lu, X.Z. Gao, L. Jiang, Z.N. Chen, T.M. Wang, J.C. Jie, H.J. Kang, Y.B. Zhang, S. Guo, H.H. Ruan, Y.H. Zhao, Z.Q. Cao, T.J. Li, Directly cast bulk eutectic and near-eutectic high entropy alloys with balanced strength and ductility in a wide temperature range, Acta Mater. 124 (2017) 143–150.
[17] M.D. Zhang, L.J. Zhang, J.T. Fan, G. Li, P.K. Liaw, R.P. Liu, Microstructure and enhanced mechanical behavior of the $Al_7Co_{24}Cr_{21}Fe_{24}Ni_{24}$ high-entropy alloy system by tuning the Cr content, Mater. Sci. Eng. A 733 (2018) 299–306.
[18] X. Jin, Y.X. Liang, J. Bi, B.S. Li, Non-monotonic variation of structural and tensile properties with Cr content in $AlCoCr_xFeNi_2$ high entropy alloys, J. Alloys Compd. 798 (2019) 243–248.
[19] Q. Wang, Y. Ma, B.B. Jiang, X.N. Li, Y. Shi, C. Dong, P.K. Liaw, A cuboidal B2 nanoprecipitation-enhanced body-centered-cubic alloy $Al_{0.7}CoCrFe_2Ni$ with prominent tensile properties, Scr. Mater. 120 (2016) 85–89.
[20] Y.T. Wang, W. Chen, J. Zhang, J.Q. Zhou, A quantitative understanding on the mechanical behavior of $AlCoCrFeNi_{2.1}$ eutectic high-entropy alloy, J. Alloys Compd. 850 (2021) 156610.
[21] Y.P. Lu, Y. Dong, S. Guo, L. Jiang, H.J. Kang, T.M. Wang, B. Wen, Z.J. Wang, J.C. Jie, Z.Q. Cao, H.H. Ruan, T.J. Li, A promising new class of high-temperature alloys: eutectic high-entropy alloys, Sci. Rep. 4 (2014) 6200.
[22] Y. Ma, J.M. Hao, J.C. Jie, Q. Wang, C. Dong, Coherent precipitation and strengthening in a dual-phase $AlNi_2Co_2Fe_{1.5}Cr_{1.5}$ high-entropy alloy, Mater. Sci. Eng. A 764 (2019) 138241.
[23] Y.P. Lu, Y. Dong, H. Jiang, Z.J. Wang, Z.Q. Cao, S. Guo, T.M. Wang, T.J. Li, P.K. Liaw, Promising properties and future trend of eutectic high entropy alloys, Scr. Mater. 187 (2020) 202–209.
[24] D.Y. Li, C.X. Li, T. Feng, Y.D. Zhang, G. Sha, J.J. Lewandowski, P.K. Liaw, Y. Zhang, High-entropy $Al_{0.3}CoCrFeNi$ alloy fibers with high tensile strength and ductility at ambient and cryogenic temperatures, Acta Mater. 123 (2017) 285–294.
[25] Y.Z. Shi, B. Yang, X. Xie, J. Brechtl, K.A. Dahmen, P.K. Liaw, Corrosion of $Al_xCoCrFeNi$ high-entropy alloys: Al-content and potential scan-rate dependent pitting behavior, Corros. Sci. 119 (2017) 33–45.

[26] Y.Z. Shi, L. Collins, N. Balke, P.K. Liaw, B. Yang, In-situ electrochemical-AFM study of localized corrosion of $Al_xCoCrFeNi$ high-entropy alloys in chloride solution, Appl. Surf. Sci. 439 (2018) 533–544.
[27] Y.Z. Shi, J.K. Mo, F.Y. Zhang, B. Yang, P.K. Liaw, Y. Zhao, In-situ visualization of corrosion behavior of $Al_xCoCrFeNi$ high-entropy alloys during electrochemical polarization, J. Alloys Compd. 844 (2020) 156014.
[28] C.M. Lin, H.L. Tsai, Evolution of microstructure, hardness, and corrosion properties of high-entropy $Al_{0.5}CoCrFeNi$ alloy, Intermetallics 19 (2011) 288–294.
[29] Y.Z. Shi, L. Collins, R. Feng, C. Zhang, N. Balke, P.K. Liaw, B. Yang, Homogenization of $Al_xCoCrFeNi$ high-entropy alloys with improved corrosion resistance, Corros. Sci. 133 (2018) 120–131.
[30] C. Chen, H. Zhang, S.X. Hu, R. Wei, T. Wang, Y.Y. Cheng, T. Zhang, N.L. Shi, F.S. Li, S.K. Guan, J.Z. Jiang, Influences of laser surface melting on microstructure, mechanical properties and corrosion resistance of dual-phase Cr–Fe–Co–Ni–Al high entropy alloys, J. Alloys Compd. 826 (2020) 154100.
[31] C.L. Wu, S. Zhang, C.H. Zhang, H. Zhang, S.Y. Dong, Phase evolution and cavitation erosion-corrosion behavior of $FeCoCrAlNiTi_x$ high entropy alloy coatings on 304 stainless steel by laser surface alloying, J. Alloys Compd. 698 (2017) 761–770.
[32] S.Y. Jiang, Z.F. Lin, H.M. Xu, Y.X. Sun, Studies on the microstructure and properties of $Al_xCoCrFeNiTi_{1-x}$ high entropy alloys, J. Alloys Compd. 741 (2018) 826–833.
[33] Y. Qiu, S. Thomas, D. Fabijanic, A.J. Barlow, H.L. Fraser, N. Birbilis, Microstructural evolution, electrochemical and corrosion properties of $Al_xCoCrFeNiTi_y$ high entropy alloys, Mater. Des. 170 (2019) 107698.
[34] X.R. Zhang, J. Guo, X.H. Zhang, Y.P. Song, Z.X. Li, X.F. Xing, D. Kong, Influence of remelting and annealing treatment on corrosion resistance of AlFeNiCoCuCr high entropy alloy in 3.5% NaCl solution, J. Alloys Compd. 775 (2019) 565–570.
[35] C. Xiang, Z.M. Zhang, H.M. Fu, E.H. Han, H.F. Zhang, J.Q. Wang, Microstructure and corrosion behavior of $AlCoCrFeNiSi_{0.1}$ high-entropy alloy, Intermetallics 114 (2019) 106599.
[36] T.T. Shun, Y.C. Du, Microstructure and tensile behaviors of FCC $Al_{0.3}CoCrFeNi$ high entropy alloy, J. Alloys Compd. 479 (2009) 157–160.
[37] N. Haghdadi, S. Primig, M. Annasamy, P. Cizek, P.D. Hodgson, D.M. Fabijanic, On the hot-worked microstructure of a face-centered cubic $Al_{0.3}CoCrFeNi$ high entropy alloy, Scr. Mater. 178 (2020) 144–149.
[38] R.P. Frankenthal, J. Kruger, Passivity of Metals, The Electrochemical Society, Inc., Princeton, 1978.
[39] ASTM standard G31–72, Standard Practice for Laboratory Immersion Corrosion Testing of Metals, ASTM International, West Conshohocken, 2004.
[40] J. Soltis, Passivity breakdown, pit initiation and propagation of pits in metallic materials – Review, Corros. Sci. 90 (2015) 5–22.
[41] Y.M. Tang, Y. Zuo, J.N. Wang, X.H. Zhao, B. Niu, B. Lin, The metastable pitting potential and its relation to the pitting potential for four materials in chloride solutions, Corros. Sci. 80 (2014) 111–119.
[42] D.D. Macdonald, M.C.H. McKubre, Modern Aspects of Electrochemistry, Plenum Press, New York, 1982.
[43] S. Guo, C. Ng, J. Lu, C.T. Liu, Effect of valence electron concentration on stability of fcc or bcc phase in high entropy alloys, J. Appl. Phys. 109 (2011) 103505.
[44] N.N. Greenwood, A. Earnshaw, Chemistry of the Elements, second ed., Butterworth-Heinemann, Oxford, 1997.
[45] N. Kumar, M. Fusco, M. Komarasamy, R.S. Mishra, M. Bourham, K.L. Murty, Understanding effect of 3.5 wt% NaCl on the corrosion of $Al_{0.1}CoCrFeNi$ high-entropy alloy, J. Nucl. Mater. 495 (2017) 154–163.
[46] C.W. Lu, Y.S. Lu, Z.H. Lai, H.W. Yen, Y.L. Lee, Comparative corrosion behavior of $Fe_{50}Mn_{30}Co_{10}Cr_{10}$ dual-phase high-entropy alloy and CoCrFeMnNi high-entropy alloy in 3.5 wt% NaCl solution, J. Alloys Compd. 842 (2020) 155824.
[47] Z.D. Han, N. Chen, S.Y. Lu, H.W. Luan, R.X. Peng, H.T. Xu, Y. Shao, Z. Peng, K.F. Yao, Structures and corrosion properties of the $AlCrFeNiMo_{0.5}Ti_x$ high entropy alloys, Mater. Corros. 69 (2018) 641–647.
[48] Y.J. Hsu, W.C. Chiang, J.K. Wu, Corrosion behavior of $FeCoNiCrCu_x$ high-entropy alloys in 3.5% sodium chloride solution, Mater. Chem. Phys. 92 (2005) 112–117.
[49] C.M. Lin, H.L. Tsai, H.Y. Bor, Effect of aging treatment on microstructure and properties of high-entropy $Cu_{0.5}CoCrFeNi$ alloy, Intermetallics 18 (2010) 1244–1250.
[50] C.M. Lin, H.L. Tsai, Effect of annealing treatment on microstructure and properties of high-entropy $FeCoNiCrCu_{0.5}$ alloy, Mater. Chem. Phys. 128 (2011) 50–56.
[51] W.R. Wang, J.Q. Wang, H.G. Yi, W. Qi, Q. Peng, Effect of molybdenum additives on corrosion behavior of $(CoCrFeNi)_{100-x}Mo_x$ high-entropy alloys, Entropy 20 (2018) 908.
[52] C. Wang, F. Jiang, F.H. Wang, The characterization and corrosion resistance of cerium chemical conversion coatings for 304 stainless steel, Corros. Sci. 46 (2004) 75–89.
[53] Y. Zhang, J.P. Liu, S.Y. Chen, X. Xie, P.K. Liaw, K.A. Dahmen, J.W. Qiao, Y.L. Wang, Serration and noise behaviors in materials, Prog. Mater. Sci. 90 (2017) 358–460.
[54] D. Choudhuri, S.A. Mantri, T. Alama, S. Banerjee, R. Banerjee, Precipitate-dislocation interaction mediated Portevin-Le Chatelier-like effect in a beta-stabilized Ti-Mo-Nb-Al alloy, Scr. Mater. 124 (2016) 15–20.